SCIENCE CHINA
Physics, Mechanics & Astronomy

• Article •

June 2023 Vol. 66 No. 6: 269611
https://doi.org/10.1007/s11433-022-2107-4

Ground-layer adaptive optics for the New Vacuum Solar Telescope: Instrument description and first results

Lanqiang Zhang[1,2], Hua Bao[1,2], Xuejun Rao[1,2], Youming Guo[1,2], Libo Zhong[1,2], Xian Ran[1,2,3], Nanfei Yan[1,2,3], Jinsheng Yang[1,2], Cheng Wang[1,2], Jiahui Zhou[1,2,3], Ying Yang[1,2,3], Yunyao Long[1,2], Xinlong Fan[1,2], Zhongyi Feng[1,2], Donghong Chen[1,2], and Changhui Rao[1,2,3*]

[1] *The Key Laboratory on Adaptive Optics, Chinese Academy of Sciences, Chengdu 610209, China;*
[2] *The Laboratory on Adaptive Optics, Institute of Optics and Electronics, Chinese Academy of Sciences, Chengdu 610209, China;*
[3] *University of Chinese Academy of Sciences, Beijing 100049, China*

Received November 18, 2022; accepted March 27, 2023; published online May 6, 2023

Ground-layer adaptive optics (GLAO) has shown its potential for use in solar observation owing to its wide field-of-view (FOV) correction. A high-order GLAO system that consists of a multiple direction Shack-Hartmann wavefront sensor (WFS), a real-time controller with a multi-CPU processor, and a 151-element deformable mirror was developed for the 1-m New Vacuum Solar Telescope at Yunnan Observatories, Chinese Academy of Sciences. A hexagonal microlens with 9×8 subapertures is employed in the WFS. The detection FOV is $42'' \times 37''$, in which 9 (3×3) guide regions are extracted for multiple direction wavefront sensing with a frame rate of up to 2200 Hz. To our knowledge, this is the first professional solar GLAO system used as a regularly operating instrument for scientific observations. Its installation and adjustment were performed in the summer of 2021. In this article, a detailed account of the GLAO system and its first light results and a comprehensive analysis of the performance of the GLAO system are provided. The results show that this system can effectively improve the imaging quality after compensating for the wavefront aberration due to ground-layer turbulence.

adaptive and segmented optics, solar instruments, astronomical observations

PACS number(s): 95.75.Qr, 95.55.Ev, 95.85.Kr

Citation: L. Zhang, H. Bao, X. Rao, Y. Guo, L. Zhong, X. Ran, N. Yan, J. Yang, C. Wang, J. Zhou, Y. Yang, Y. Long, X. Fan, Z. Feng, D. Chen, and C. Rao, Ground-layer adaptive optics for the New Vacuum Solar Telescope: Instrument description and first results, Sci. China-Phys. Mech. Astron. **66**, 269611 (2023), https://doi.org/10.1007/s11433-022-2107-4

1 Introduction

Adaptive optics (AO) has been extensively used in large-aperture solar telescopes, such as the 1-m New Vacuum Solar Telescope (NVST) [1], 1.6-m Goode Solar Telescope (GST, also named "NST" before July 17, 2017) [2], 1.5-m GREGOR telescope [3], 1.8-m Chinese Large Solar Telescope [4], and 4-m Daniel K. Inouye Solar Telescope [5], to acquire high-resolution solar photospheric and chromospheric images. However, due to the vertical distribution of the turbulence, conventional AO (CAO) generally has a small corrected field-of-view (FOV) [6]. This corrected FOV is called the isoplanatic angle, with a typical size of the order of 5″-15″ for solar observations in the visible-light regime at good telescope sites [7]. A typical solar active region extends up to 7′ [8-10], including complex dynamic structures,

*Corresponding author (email: chrao@ioe.ac.cn)

such as sunspots, filaments and plages. Large-FOV AO such as multi-conjugate AO (MCAO) [11] and ground-layer AO (GLAO) [12], which is also called the next-generation AO, were proposed to achieve the observation requirement with large FOV and high resolution. Both techniques are based on the stratification of atmospheric turbulence and the idea of layered compensation. Compared with MCAO, GLAO is generally used to improve the image quality for large-aperture ground-based optical telescopes across a wide FOV. The homogeneous imaging performance would be obtained by compensating the aberration from the ground-layer turbulence. The fact that about 60% of the turbulence strength is concentrated in the first few kilometers above the telescope makes this concept attractive for solar observations that require homogeneous image quality improvement over a wide FOV rather than a diffraction-limited resolution [13]. The potential of GLAO with post-image process to produce diffraction-limited images has been demonstrated [14].

In 2001, F. Rigaut proposed the concept of GLAO for the problem of large-FOV imaging with the Extremely Large Telescope. Many studies have shown that atmospheric turbulence is mainly concentrated in the ground-layer up to an altitude of tens to hundreds of meters for many excellent observation sites, making GLAO very feasible [15,16]. The advantages of GLAO are obvious, and the scientific goal of high-resolution imaging with a large FOV can still be achieved with reduced system complexity.

GLAO systems are developed and commissioned on-sky for many ground-based night-time astronomical telescopes, such as the SOAR telescope with a $3' \times 3'$ FOV [17], the Large Binocular Telescope with a $4' \times 4'$ FOV [18], and the Very Large Telescope with a $7' \times 7'$ FOV [19]. Recent results with the Imaka telescope show an optimized image quality better than $0.15''$ full width at half maximum over the central $11' \times 11'$ FOV [20].

The uniform correction across an extra-large FOV makes GLAO an attractive option for solar telescopes and some scientific applications [21]. Up to now, there is no professional GLAO system for solar observations. A series of MCAO experiments were performed on solar telescopes, such as the Vacuum Tower Telescope (VTT), Dunn Solar Telescope, GREGOR telescope, and GST [22-25]. At least two deformable mirrors (DMs) are employed in MCAO to correct the low-altitude turbulence wavefront distortions and high-altitude turbulence. GLAO was tested if one just controls the ground-layer conjugated DM for the correction. In this case, the maximum FOV of the by-product GLAO system is limited by the detector size of the MCAO system. Moreover, as the wavefront sensor (WFS) needs to be placed behind the high-altitude correction DMs, non-common path aberration will be relatively enlarged.

We developed a GLAO prototype system at the 1-m NVST and obtained the first light in January 2016 [26]. A multiple-direction Shack-Hartmann wavefront sensor (MD-WFS) with 7×7 subaperture arrays and a CMOS high-speed camera Mikrotron EoSens MC1362 was employed to detect the ground-layer aberration. A real-time controller (RTC) was developed based on a field-programmable gate array (FPGA) and multicore digital signal processor (DSP). The maximum frame frequency was approximately 840 Hz at that time. Afterward, we started to develop a professional GLAO system with high-order correction for routine operation at the NVST.

In this article, we introduce the system in detail and its first light results and conduct a comprehensive analysis of the performance of the GLAO system. This paper is organized as follows: in sect. 2, the GLAO system is described in detail. In sect. 3, the first light results are given. In sect. 4, the system performance analysis is presented. In sect. 5, the main conclusions are given.

2 Instrument description

2.1 Optical layout

The optical layout of the GLAO system is shown in Figure 1. The part enclosed by the chain-dotted line is inherited from the 151-element AO system [6]. The correlation Shack-Hartmann WFS was upgraded to an MD-WFS, which simultaneously detects wavefront aberrations from different lines of sight. The correlation Shack-Hartmann WFS was retained for the CAO correction mode,which is not shown here. Moreover, a science imaging channel with the wavelength band of TiO was placed for recording the high-resolution images after GLAO correction and evaluating the system performance.

2.2 Wavefront sensor

MD-WFS has been widely used in solar AO. It was first proposed by Soltau et al. [27] when they developed the MCAO experiments at the VTT. Each subaperture of MD-WFS corresponds to a large FOV, normally 1 arcmin. Multiple guide regions (GRs) corresponding to different lines of sight are extracted from the subimage array of the MD-WFS. The subimages from the same direction are reformed as a new subimage array and used to measure the wavefront from that line of sight. Based on this method, the wavefront aberrations in the pupil place from multiple directions could be simultaneously measured using MD-WFS.

For GLAO, the simple way to obtain wavefront aberrations caused by ground-layer turbulence is to average the multiple

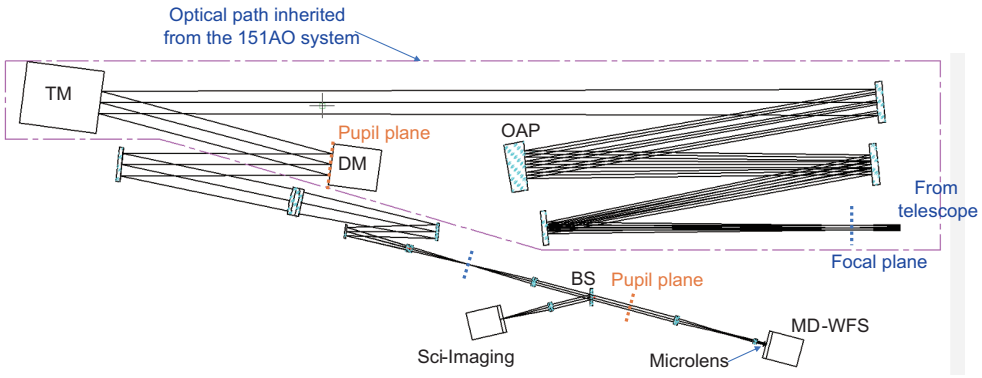

Figure 1 (Color online) Optical layout of the GLAO system. DM: deformable mirror, TM: tilt mirror, OAP: off-axis parabolic mirror, BS: beam splitter.

direction detecting results. The light rays from different lines of sight pass through a similar place in the ground-layer and separate further as the altitude increases. Hence, the aberration from the high-altitude turbulence could be removed after the wavefront average, and the part from the ground-layer turbulence is retained.

The detected thickness of the ground-layer affects the correction performance after GLAO correction. It is related to the FOV of the wavefront sensing for a certain telescope. The transmission paths for different lines of sight would have more overlaps for small-FOV wavefront sensing. The remaining aberrations after the average contain the wavefront error from the high-layer turbulence. This is similar to the correction effect of CAO. With the expansion of the detecting FOV, the residual wavefront error corresponding to the high-level turbulence will be increasingly less among the mean wavefront. The uniformity across the FOV after GLAO correction would be better, whereas the correction gain decreases. Therefore, GLAO is a trade-off process between the correction FOV and gain, which improves the correction effect of a larger FOV by sacrificing the correction resolution of the central FOV. This process is directly related to the parameters of the WFS.

The specifications of the MD-WFS in this GLAO system are shown in Table 1. The Mikrotron 3CXP camera was selected as the detector to capture the subimage array with a wavelength of 500 ± 5 nm. Considering the dynamic characteristics of the atmospheric turbulence at the Fuxian Lake site, a detection frequency of more than 2000 Hz is needed. The aperture was sampled by a 9×8 microlens array, which cannot make the telescope reach the imaging performance of the diffraction limit. These specifications are the trade-off results in the FOV, the pixel resolution of the subimage array, and the frame rate of wavefront sensing. GLAO is a partial correction system. A 9×8 subaperture sampling could obtain good correction performance according to the simulation results. Considering the requirements of the GLAO closed loop based on solar granulation, the pixel resolution of the subimage was set to 0.6″. This is slightly bigger than the mainstream accepted as 0.5″, so that a larger detection FOV could be obtained based on a given pixel size of the detector. In this system, the whole wavefront sensing FOV of $42'' \times 37''$ is adopted, and up to 9 GRs, 3×3 arrangement with a column spacing of 11.4″ and a row spacing of 8.4″ are used to participate in the aberration measurement caused by ground-layer turbulence. Each GR corresponds to $14.4'' \times 14.4''$ FOV, and there is an overlap on the subimages for extracting the GRs. The GRs could be freely selected according to the accuracy of wavefront sensing and the interested observing target. We can give up some GRs by hand if the detection accuracy decreases because of the low contrast or other reasons. Moreover, we can switch the GLAO mode to a low-order CAO by selecting one GR during wavefront sensing.

The arrangement of the subapertures and the sunspot subimages are shown in Figure 2. The GRs are shown in

Table 1 MD-WFS specifications

Parameter	Value
No. of microlens	9×8
Shape of microlens	hexagon
FOV	$42'' \times 37''$
Pixel scale	0.6″
Frame frequency	2200 Hz
Wavelength	500 ± 5 nm

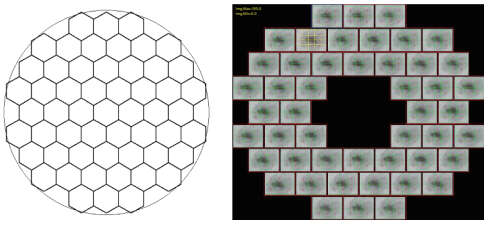

Figure 2 (Color online) Arrangement of the subapertures and subimages of the sunspot.

each subimage with a green-line diagram, and the one with a yellow line shows where the reference image is located.

2.3 Wavefront corrector

The correctors, including the tip/tilt mirror and DM, are shared with the original 151-element AO system. The diameter of the tip/tilt mirror is 90 mm, with the beam footprint size of 62 mm. The high-order DM is a 151-element piezoelectric driven mirror. The performance of the two mirrors was fully verified in the 151-element AO system. The specific parameters can be found in ref. [6].

2.4 Real-time controller

The RTC determines the temporal characteristics of the GLAO system. Two general architectures based on "FPGA+DSP" and "FPGA+Multi-CPUs" are employed as the mainstream platform of RTC [28, 29]. Both would meet our requirements, and their characteristics are as follows.

Considering the hardware resources and costs, the architecture "FPGA+DSP" occupies fewer resources, whereas the architecture "FPGA+Multi-CPUs" has a lower cost. In terms of real-time performance, "FPGA+DSP" is developed based on a custom platform and has less time delay compared to "FPGA+Multi-CPUs". However, the time delay would increase with the use of a multiple-board platform because of the inter-board communication delays. In terms of flexibility, "FPGA+Multi-CPUs" is convenient for adjusting and fits various algorithm strategies. Meanwhile, for the custom architecture, "FPGA+DSP" is usually very time-consuming for algorithm optimization. From the perspective of the development cycle, "FPGA+Multi-CPUs", which is based on a common platform, is fast for developing and has easy maintenance.

In this GLAO system, the "FPGA+Multi-CPUs" architecture was adopted. To meet the demand of the timing delay and jitter for real-time computation, the RTC platform of a real-time control system is a custom-built architecture based on an x86 computing server of a 48-core CPU with a Linux CentOS 8.2 operating system. Two advanced Xilinx-series FPGA cards are also employed, one for digital data acquisition and another for digital data I/O. The real-time processing is depicted in Figure 3, in which MD-WFS images are acquired by an FPGA acquisition card, tip-tilt & DM control signals are transformed by an FPGA digital I/O card to a high-voltage amplifier, and dark & flat field preprocess, CC computation, parabolic interpolation, wavefront reconstruction, and proportional-integral-differential servo control are accomplished in a multicore CPU.

The WFS detector delivers 8-bit per-pixel data in a region of 576×561 pixels at a frame rate of 2200 Hz. The geometry arrangement of a subaperture is 9×8, and the effective subaperture number is 48. The slope calculation, wavefront reconstruction, and voltage restoration operations are decomposed into multiple independent threads and distributed to each physical core. The PV operation of semaphores is used to realize the concurrency of each thread. The message-driven mechanism is adopted to avoid deadlocks. Through these processes, the average timing delay is less than 500 μs, and a computing jitter of approximately ±50.0 μs is achieved, with the condition that nine GRs are fully used for large-FOV wavefront detection. For the system control, the modal control method is indispensable, and up to 45 Zernike modes are used for a GLAO closed loop (the first 27-order Zernike aberrations were corrected during the first light observation). The TM and DM are controlled by the MD-WFS, and the average tit/tilt errors from different GRs are used for the closed loop of the tip/tilt tracker.

3 Observational results in the first light

The GLAO system was integrated into the Coud room of the NVST in 2021. Figure 4 displays short-exposure images of sunspots and granulations in the TiO band (7057 Å, 7 Å) before and after GLAO correction, which were taken during the first light observation on August 29, 2021. The speckle image reconstruction of the GLAO image sequence is shown correspondingly. The open- and closed-loop images of the sunspots were obtained at 06:53:42 and 06:47:23 UT, respectively. The open- and close-loop images of the granulations were obtained at 07:44:25 and 07:42:51 UT, respectively.

From these figures, one can find the improvement of the spatial resolution after GLAO closed loop and reconstruction. The images after GLAO correction have higher contrast and reveal finer structures.

4 System performance evaluation

The system performance evaluation was performed based on the granulation image sequence above. The long-exposure image and its contrast, generalized Fried parameters r_0, and image motion were adopted for evaluating the imaging performance, and the power spectral densities (PSDs) of different Zernike-order aberrations are given to describe the control characteristics. The GLAO system was mounted on the telescope in the summer of 2021, and a trial observation was performed afterward. The slope and voltage information during observation were saved in real time for the profile mea-

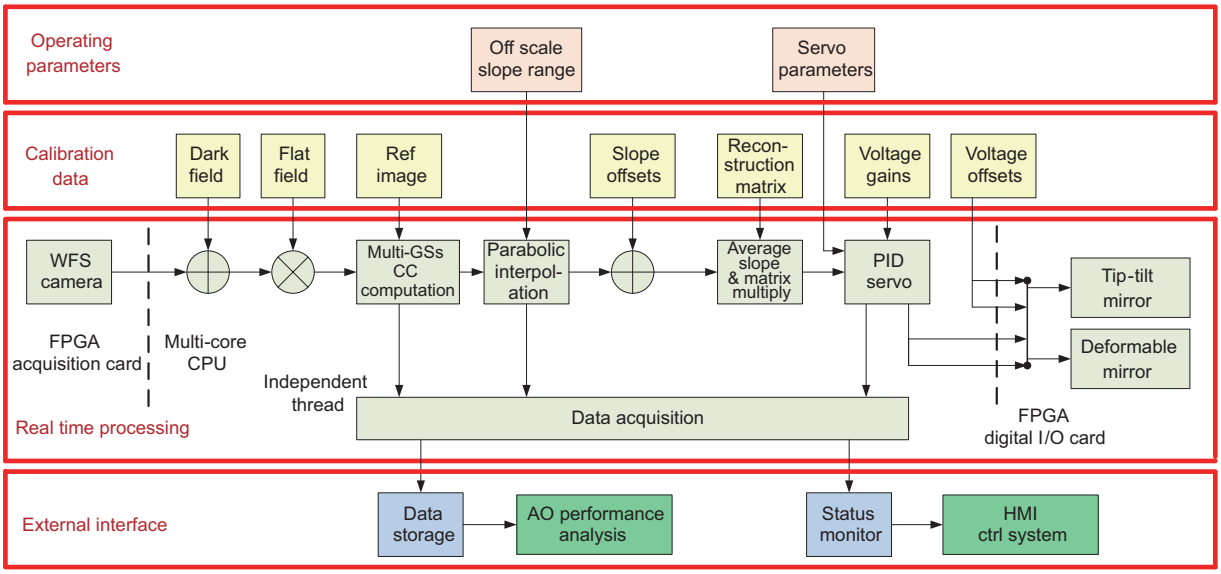

Figure 3 (Color online) Block diagram of a real-time processor.

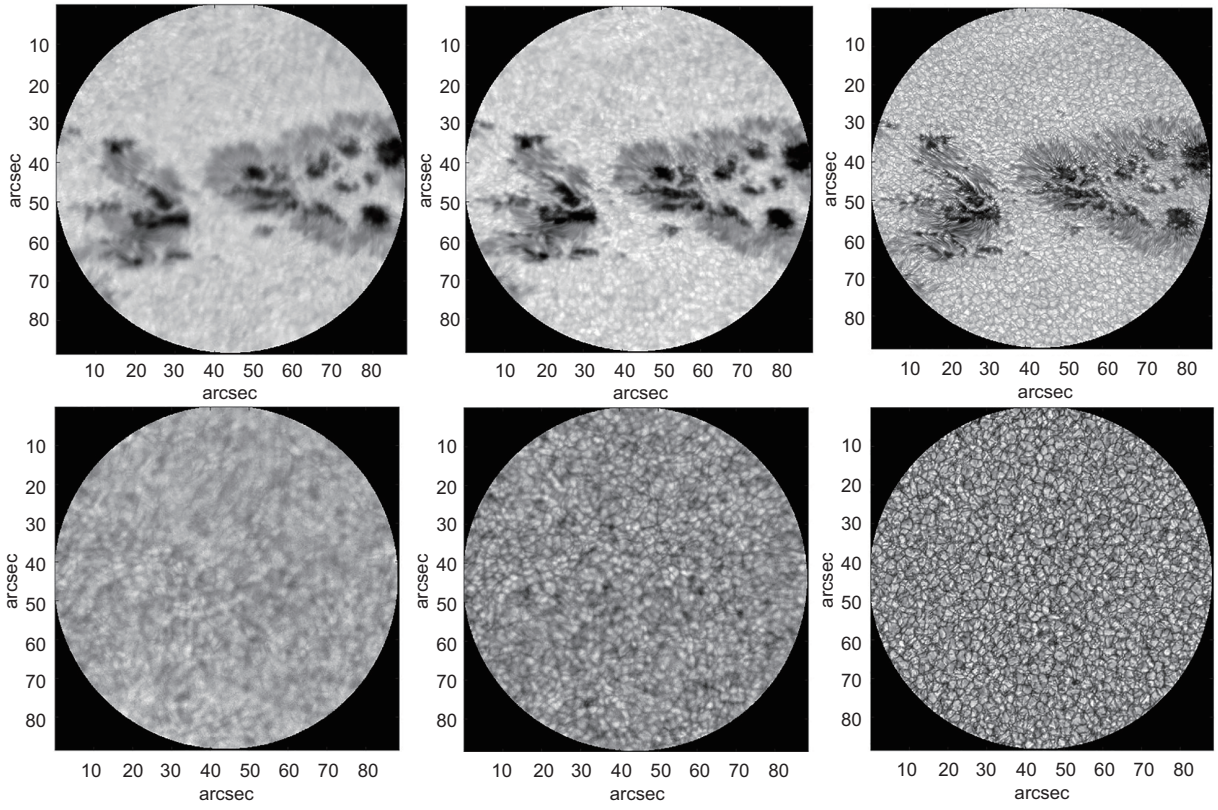

Figure 4 Short-exposure images of sunspots before and after GLAO correction and speckle reconstruction images.

surement of optical turbulence and the system performance evaluation. All the subsequent analyses and evaluations are based on the data record from 6:45 to 7:50 UT on August 29 when the GLAO system was tested for different work modes. The seeing during this time was measured based on the slope and voltage data. Then, the tracking and GLAO correction performance were evaluated.

Figure 5 shows the histogram of the Fried parameter at the time between 6:45 and 7:50 UT on August 29, 2021 with the open and close data. The average seeing during this period is approximately 9.18 cm. This result was calculated from the saved slope and voltage data. For the data saved in the

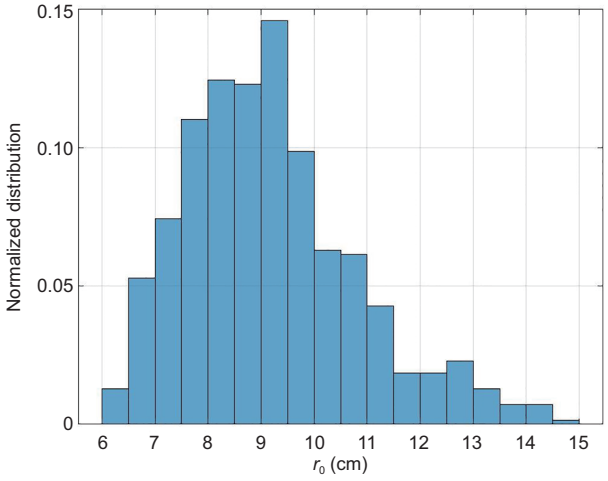

Figure 5 (Color online) r_0 distribution corresponding to open-loop data from 6:45 to 7:50 UT on August 29, 2021.

closed-loop state, the corresponding open-loop data were obtained using the pseudo-open-loop reconstruction method [30], and the seeing was calculated based on the pseudo-open-loop data. The DIMM [31] method was used for calculating the seeing. During the calculation process, some obviously incorrect data were eliminated. As shown in the results in the figure, the seeing changes between 6 and 15 cm during the corresponding observed time, and mainly concentrates between 7 and 11 cm. The seeing greatly fluctuates, which is a huge challenge to the stability of the GLAO correction.

4.1 Imaging performance

The long-exposure image of granulation from 200-frame short-exposure images is shown in Figure 6. The RMS contrasts of the subfields (FOV is 2.36″) at the long-exposure image before and after GLAO correction are also displayed, and the mean contract is improved from 1.6% to 2.8%.

Estimating the imaging quality of extended objects after the GLAO correction was not directly performed as in the stellar case. To quantitatively illustrate the GLAO performance from the images, the generalized Fried parameter [32, 33] is usually used. The generalized Fried parameter is an estimation of the Fried parameter [34] when the correction is applied. The distributions of generalized Fried parameters across the whole FOV calculated from the GLAO-off and GLAO-on image sequence are given in Figure 7. The unit of the color tables is meter. Without GLAO, the mean value of the generalized Fried parameters is about approximately 9.29 cm at the TiO band, and the image quality is uniform across the whole FOV. With GLAO correction, the mean value of the generalized Fried parameters increased to 13.42 cm.

To estimate the correction ability of the GLAO system, the residual image motion of the individual isoplanatic subfields in the closed-loop image over 100 time steps was measured after the compensation of the overall image motion based on the far-field image sequence [35]. The image with the maximum RMS contrast value in the sequence was chosen as the reference image in the calculation. The image motion is based on locating the cross-correlation maximum of the individual isoplanatic subfield with the corresponding reference subfield. The subfield with the lowest residual image jitter variance is the lock point of the GLAO system. As shown in Figure 8 the measured RMS errors of the image motion with the unit of pixels are presented for the different subfields. Compared with open images, the average image motion across the FOV after GLAO correction was reduced from 5.88 to 1.9 pixels. The values were calculated from overlapping subfields in size of $2.36'' \times 2.36''$ corresponding to 64×64 pixels in the high-resolution images. The subfields contain enough details and an adequate signal-to-noise ratio for the calculation of cross-correlation. The overlap is not considered in Figure 8, and the dark shades correspond to low variance.

As shown in the distribution of the generalized Fried parameter and image motions, the correction effect is obvious in the FOV of 30″, which relates to the detection FOV of different GRs in the MD-WFS, whereas the effect in the area outside the detecting FOV is inconspicuous. This correction non-uniformity is related to the GR layout. The GRs would contribute different weights, and some research about layout optimization is performed to determine the uniformity correction effect across the FOV. Because the improvement of the resolution by the GLAO is limited and field dependent, a speckle imaging technique with field-dependent speckle transfer functions is needed for further improving the quality of the whole FOV image [14].

4.2 Controlling characteristics

The fine-tracking technology is very mature and has been proved in the 151-element AO system to correct the global tilt and stabilize image motion. However, an individual tracking detector in this system was employed for the global tilt measurement. In the GLAO system, the tracking detector was eliminated. The first two-order Zernike errors measured by MD-WFS were used for the fine-tracking loop. Aside from the tip-tilt, the remaining 25 higher-order Zernike modes were compensated by the DM.

The time-domain analysis of the tracking correction error and higher-order correction residual error of GLAO are displayed in Figure 9. Compared with the open loop, the precision tracking closed loop of GLAO effectively suppressed

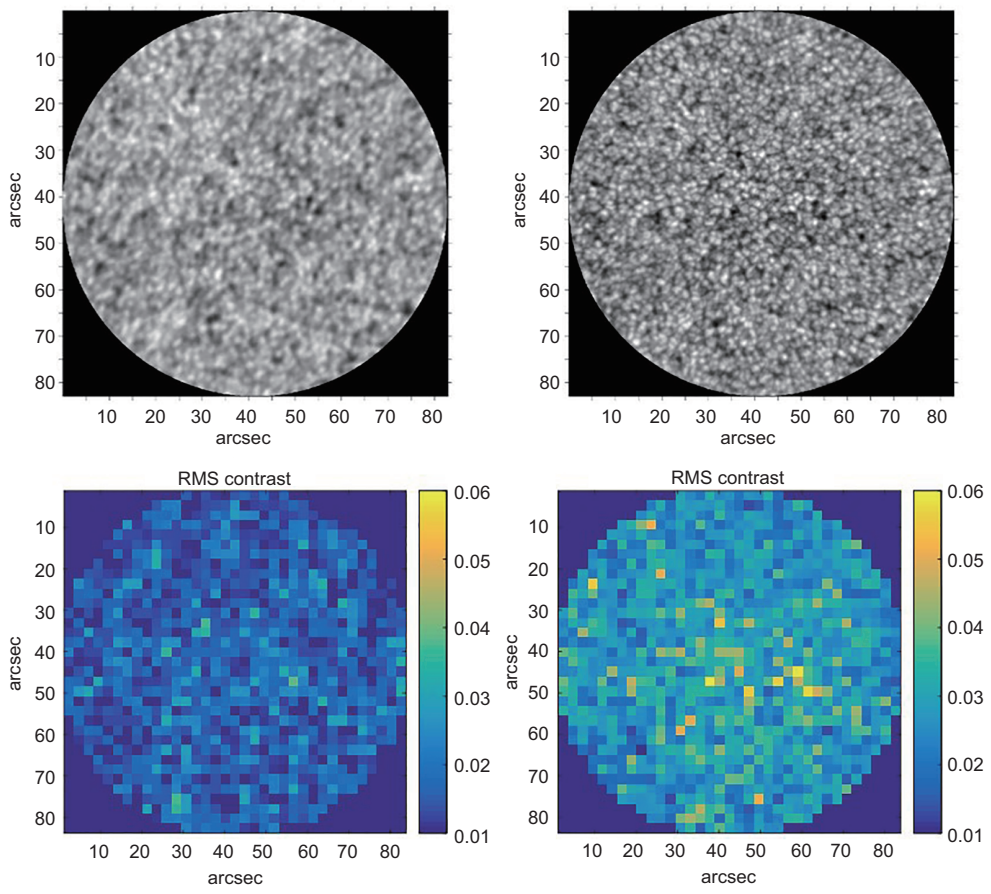

Figure 6 (Color online) Long-exposure images of granulation before and after GLAO correction and the corresponding RMS contrasts of the subfields (FOV is 2.36″).

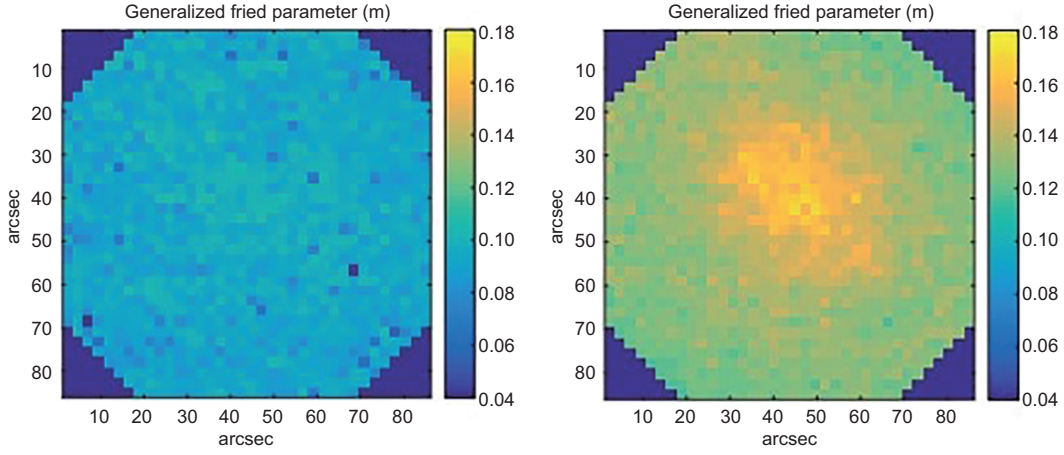

Figure 7 (Color online) Distribution of the generalized Fried parameter for each isoplanatic patch encoded as a gray-scale map across the whole FOV calculated from the open-loop image sequence (left) and GLAO image sequence (right).

the error on the tip-tilt component, the x-tilt decreased by approximately 11, and the y-tilt was reduced by a factor of 4. In addition, as shown in the bottom part of the figure, the RMS error of the high-order aberrations in the GLAO system decreased from approximately 194 to 49 nm on average.

To further illustrate the performance after correction, the PSDs of the 1st (tip), 2nd (tilt), 3rd (focus), and 15th Zernike orders with the GLAO open and closed loop are shown in Figure 10.

The falloffs of the high frequency of the PSDs follow a power law with an exponent of −8/3. The PSD curves of fre-

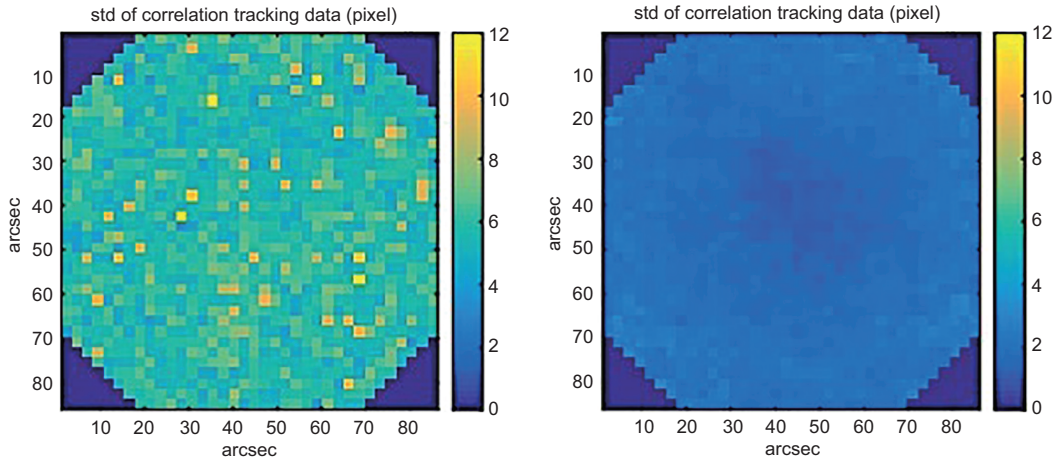

Figure 8 (Color online) Standard deviation distribution of the residual image motion of individual isoplanatic subfields at the sequence before (left) and after (right) the GLAO correction.

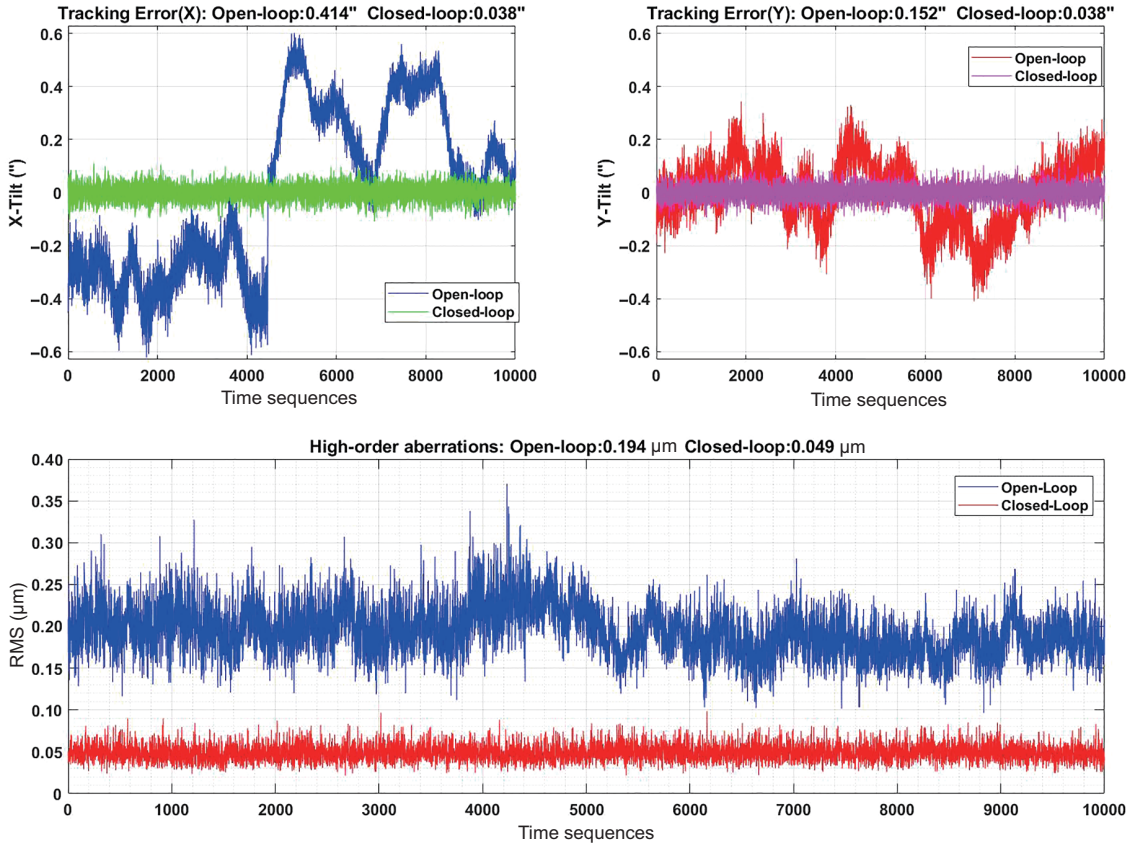

Figure 9 (Color online) Temporal tracking errors and high-order aberrations. The sunspots were used as the GRs, and the detection time is August 29, T06:53:41 for the open loop and T06:47:23 for the closed loop.

quencies above 400 Hz look like a floor and are mainly determined by the measurement noise. The PSDs of the Zernike modes with AO-on are equivalent to the PSDs of white noise. These results demonstrate that the temporal error has been corrected to a very small level.

The error transfer functions are shown in Figure 11. The cross frequency between the function curve and 0 dB line represents the suppression bandwidth. The top row indicates that the bandwidth of the x-tilt and y-tilt correction is close to 70 Hz. Meanwhile, the bottom panel reveals that the error rejection bandwidth of the high-order correction is approximately 77 Hz.

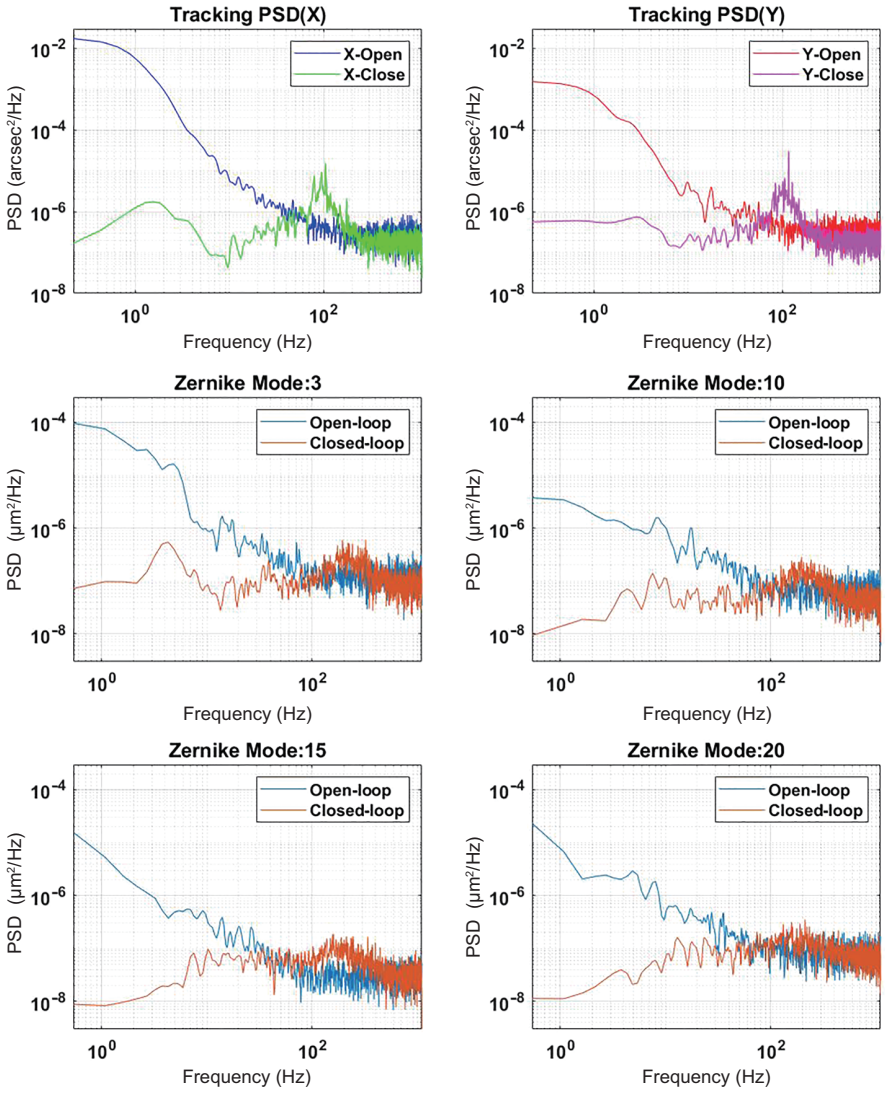

Figure 10 (Color online) GLAO-off and GLAO-on PSDs. The crossover frequencies of the two curves indicate the error rejection bandwidths.

5 Discussion and conclusions

This paper describes the design and performance of a professional solar GLAO system developed and mounted at the NVST in the summer of 2021. In general, an MD-WFS was employed for detecting the turbulence aberration caused by the ground-layer. An RTC based on the multicore CPU platform was simultaneously developed to calculate the wavefront error of up to 9 GRs. Moreover, the tracker in the fine-tracking loop of the CAO system was removed, and the first two Zernike modes from MD-WFS were extracted for the tip/tilt mirror control. The RTC could run the GLAO system with 2200 Hz. The GLAO could compensate for the turbulence with up to 45 Zernike modes. The error rejection bandwidth of the fine-tracking loop and high-order GLAO correction (3-27 Zernike modes were used in the test) could be up to 70 and 77 Hz, respectively.

Based on the normalized r_0 and residual image motion, the image quality improvement throughout the whole FOV after the GLAO correction and the correction effect in the central FOV are better than those in the edge part. This condition is limited by the GR layout, and is corroborated by simulation calculations. In the next step, we will improve the consistency of the system correction performance by optimizing the GR layout.

The GLAO system has been successfully used with the grating spectrograph at the NVST, which can help stabilize the image on the slit of the spectrograph. Relevant results will be reported in the future. With the help of GLAO, it is expected to obtain good spectral data and improve the scientific productivity of the NVST. The system is also planned to work with the multiple-channel high-resolution imaging

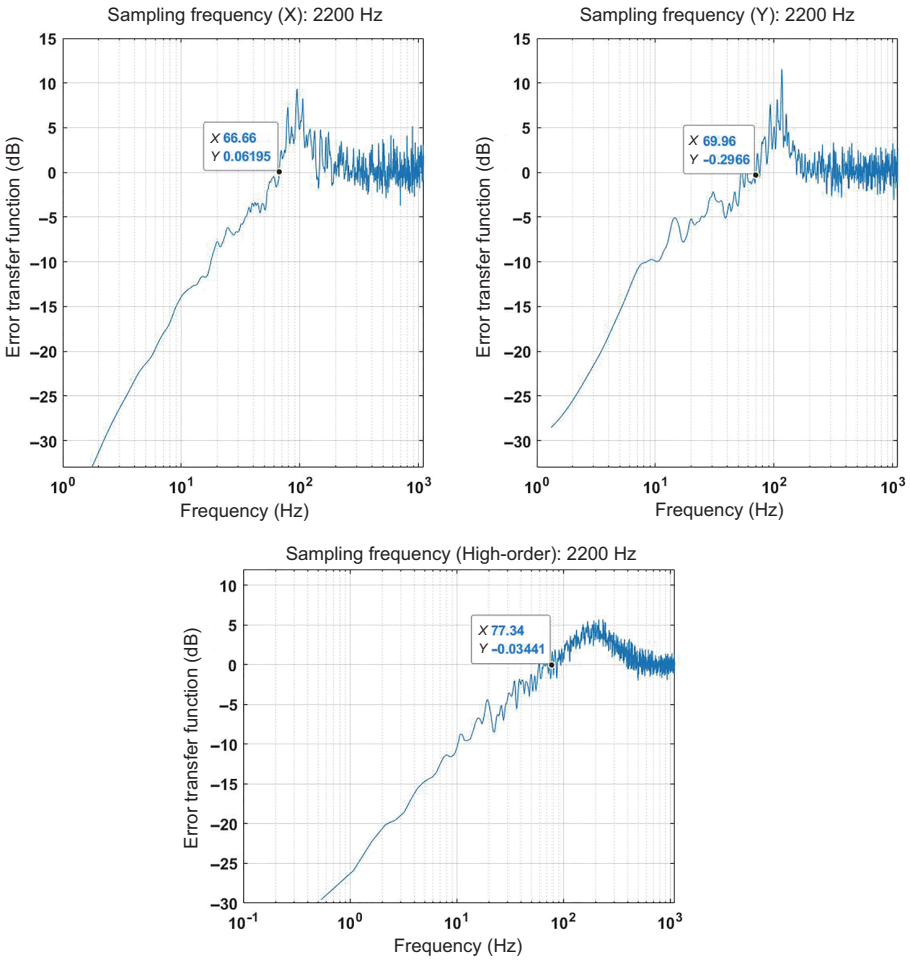

Figure 11 (Color online) Error transfer functions.

system, and the diffraction-limited image would be expected with the combination of the GLAO correction and post-facto image reconstruction.

This work was supported by the National Natural Science Foundation of China (Grant Nos. 11727805, and 12103057), Frontier Research Fund of Institute of Optics and Electronics, Chinese Academy of Sciences (Grant No. C21K002), and Youth Innovation Promotion Association of the Chinese Academy of Sciences (Grant Nos. 2021378, 2020376, and 2022386). The authors are grateful to Prof. Jun Xu and his team at Yunnan Astronomical Observatory for their help during the system assembly and on-sky observations. The authors would also like to thank Mr. Xuean Ma, retired mechanical engineer, for his contribution in system adjustment and alignment.

1 Z. Liu, J. Xu, B. Z. Gu, S. Wang, J. Q. You, L. X. Shen, R. W. Lu, Z. Y. Jin, L. F. Chen, K. Lou, Z. Li, G. Q. Liu, Z. Xu, C. H. Rao, Q. Q. Hu, R. F. Li, H. W. Fu, F. Wang, M. X. Bao, M. C. Wu, and B. R. Zhang, Res. Astron. Astrophys. **14**, 705 (2014).
2 P. R. Goode, and W. Cao, *The 1.6 m off-axis New Solar Telescope (NST) in Big Bear, Ground-based and Airborne Telescopes IV* (Amsterdam, 2012).
3 W. Schmidt, O. von der Lühe, R. Volkmer, C. Denker, S. K. Solanki, H. Balthasar, N. Bello González, T. Berkefeld, M. Collados, A. Fischer, C. Halbgewachs, F. Heidecke, A. Hofmann, F. Kneer, A. Lagg, H. Nicklas, E. Popow, K. G. Puschmann, D. Schmidt, M. Sigwarth, M. Sobotka, D. Soltau, J. Staude, K. G. Strassmeier, and T. A. Waldmann, Astron. Nachr. **333**, 796 (2012).
4 C. H. Rao, N. T. Gu, X. J. Rao, C. Li, L. Q. Zhang, J. L. Huang, L. Kong, M. Zhang, Y. T. Cheng, Y. Pu, H. Bao, Y. M. Guo, Y. Y. Liu, J. S. Yang, L. B. Zhong, C. J. Wang, K. Fang, X. J. Zhang, D. H. Chen, C. Wang, X. L. Fan, Z. W. Yan, K. L. Chen, X. Y. Wei, L. Zhu, H. Liu, Y. J. Wan, H. Xian, and W. L. Ma, Sci. China-Phys. Mech. Astron. **63**, 109631 (2020).
5 T. R. Rimmele, M. Warner, S. L. Keil, P. R. Goode, M. Knölker, J. R. Kuhn, R. R. Rosner, J. P. McMullin, R. Casini, H. Lin, F. Wöger, O. von der Lühe, A. Tritschler, A. Davey, A. de Wijn, D. F. Elmore, A. Fehlmann, D. M. Harrington, S. A. Jaeggli, M. P. Rast, T. A. Schad, W. Schmidt, M. Mathioudakis, D. L. Mickey, T. Anan, C. Beck, H. K. Marshall, P. F. Jeffers, J. M. Oschmann Jr., A. Beard, D. C. Berst, B. A. Cowan, S. C. Craig, E. Cross, B. K. Cummings, C. Donnelly, J. B. de Vanssay, A. D. Eigenbrot, A. Ferayorni, C. Foster, C. A. Galapon, C. Gedrites, K. Gonzales, B. D. Goodrich, B. S. Gregory, S. S. Guzman, S. Guzzo, S. Hegwer, R. P. Hubbard, J. R. Hubbard, E. M. Johansson, L. C. Johnson, C. Liang, M. Liang, I. McQuillen, C. Mayer, K. Newman, B. Onodera, L. E. Phelps, M. M. Puentes, C. Richards, L. M. Rimmele, P. Sekulic, S. R. Shimko, B. E. Simison, B. Smith, E. Starman, S. R. Sueoka, R. T. Summers, A. Szabo, L. Szabo, S. B. Wampler, T. R. Williams, and C. White, Sol. Phys. **295**, 172 (2020).
6 C. Rao, L. Zhu, X. Rao, L. Zhang, H. Bao, L. Kong, Y. Guo, L. Zhong, X. Ma, M. Li, C. Wang, X. Zhang, X. Fan, D. Chen, Z. Feng, N. Gu, and Y. Liu, Astrophys. J. **833**, 210 (2016).
7 T. R. Rimmele, and J. Marino, Living Rev. Sol. Phys. **8**, 2 (2011).

8 H. Q. Zhang, Sci. China-Phys. Mech. Astron. **63**, 119611 (2020), arXiv: 2009.03573.
9 D. Li, J. Xue, D. Yuan, and Z. Ning, Sci. China-Phys. Mech. Astron. **65**, 239611 (2022), arXiv: 2201.07535.
10 Y. W. Ni, J. H. Guo, Q. M. Zhang, J. L. Chen, C. Fang, and P. F. Chen, Astron. Astrophys. **663**, A31 (2022), arXiv: 2203.15660.
11 S. Esposito, Compte. Rendus. Phys. **6**, 1039 (2005).
12 F. Rigaut, in *Ground Conjugate Wide Field Adaptive Optics for the ELTs, European Southern Observatory Conference and Workshop Proceedings* (Venice, 2002).
13 D. Schmidt, N. Gorceix, P. R. Goode, J. Marino, T. Rimmele, T. Berkefeld, F. Wöger, X. Zhang, F. Rigaut, and O. von der Lühe, Astron. Astrophys. **597**, L8 (2017).
14 L. Zhong, L. Zhang, Z. Shi, Y. Tian, Y. Guo, L. Kong, X. Rao, H. Bao, L. Zhu, and C. Rao, Astron. Astrophys. **637**, A99 (2020).
15 P. G. Kovadlo, V. P. Lukin, A. Y. Shikhovtsev, in *Towards improvements of the adaptive optics systems in astronomy, 26th International Symposium on Atmospheric and Ocean Optics, Atmospheric Physics* (Moscow, 2020).
16 M. Chun, in *First results with 'imaka, SPIE Astronomical Telescopes + Instrumentation 2016-Adaptive Optics for Extremely Large Telescopes 5* (Edinburgh, 2017).
17 A. Tokovinin, R. Cantarutti, R. Tighe, P. Schurter, M. Martinez, S. Thomas, and N. van der Bliek, PASP **128**, 125003 (2016), arXiv: 1608.05593.
18 G. Orban de Xivry, S. Rabien, L. Busoni, W. Gaessler, M. Bonaglia, J. Borelli, M. Deysenroth, S. Esposito, H. Gemperlein, M. Kulas, M. Lefebvre, T. Mazzoni, D. Peter, A. Puglisi, W. Raab, G. Rahmer, A. Sivitilli, J. Storm, and J. Ziegleder, *First on-sky results with ARGOS at LBT, SPIE Astronomical Telescopes + Instrumentation-Conference on Adaptive Optics Systems V* (Edinburgh, 2016).
19 P. La Penna, E. Aller Carpentier, J. Argomedo, R. Arsenault, R. D. Conzelmann, B. Delabre, R. Donaldson, F. Gago, P. Gutierrez-Cheetam, N. Hubin, P. Jolley, M. Kiekebusch, J. P. Kirchbauer, B. Klein, J. Kolb, H. Kuntschner, M. Le Louarn, J.-L. Lizon, P.-Y. Madec, A. Manescau, L. Mehrgan, S. Oberti, J. Quentin, B. Sedghi, S. Ströbele, M. Suárez Valles, C. Soenke, S. Tordo, and J. Vernet, *AOF: Standalone test results of GALACSI, SPIE Astronomical Telescopes + Instrumentation-Conference on Adaptive Optics Systems V* (Edinburgh, 2016).
20 M. R. Chun, O. Lai, D. Toomey, J. R. Lu, M. Service, C. Barane, S. Thibault, D. Brousseau, Y. Hayano, S. Oya, S. Santi, C. Kingery, K. Loss, J. Gardiner, and B. Steele, *Imaka: A ground-layer adaptive optics system on Maunakea, SPIE Astronomical Telescopes + Instrumentation-Conference on Adaptive Optics Systems V* (Edinburgh, 2016).
21 Y. Yang, L. Zhang, and C. Rao, Mon. Not. R. Astron. Soc. **518**, 3201 (2022).
22 T. Berkefeld, D. Soltau, O. Von Der Luehe, in *Results of the multi-conjugate adaptive optics system at the German solar telescope, Tenerife, Astronomical Adaptive Optics Systems and Applications II* (San Diego, 2005).
23 T. R. Rimmele, K. Richards, J. M. Roche, S. Hegwer, A. Tritschler, in *Progress with solar multi-conjugate adaptive optics at NSO, Proceedings of SPIE - The International Society for Optical Engineering* (Orlando, 2006).
24 D. Schmidt, T. Berkefeld, F. Heidecke, A. Fischer, Q. von der Lühe, and D. Soltau, *GREGOR MCAO looking at the Sun, SPIE Astronomical Telescopes + Instrumentation-Conference on Adaptive Optics Systems IV* (Montreal, 2014).
25 D. Schmidt, N. Gorceix, J. Marino, T. Berkefeld, T. Rimmele, X. Zhang, F. Wöger, and P. Goode, *Progress in multi-conjugate adaptive optics at Big Bear Solar Observatory, SPIE Astronomical Telescopes + Instrumentation-Conference on Adaptive Optics Systems V* (Edinburgh, 2016).
26 L. Kong, L. Zhang, L. Zhu, H. Bao, Y. Guo, X. Rao, L. Zhong, and C. Rao, Chin. Opt. Lett. **14**, 100102 (2016).
27 D. Soltau, T. Berkefeld, O. V. D. Lühe, F. Wöger, and T.h. Schelenz, Astron. Nachri. **323**, 236 (2002).
28 L. Kong, L. Zhu, L. Zhang, H. Bao, and C. Rao, IEEE. Photon. J. **9**, 1 (2017).
29 D. Jenkins, *A Prototype Adaptive Optics Real-Time Control Architecture for Extremely Large Telescopes using Many-Core CPUs*, Dissertation for the Doctoral Degree (Durham University, Durham, 2019).
30 P. Piatrou, and L. Gilles, Appl. Opt. **44**, 1003 (2005).
31 M. Sarazin, and F. Roddier, Astron. Astrophys. **227**, 294 (1990).
32 O. von der Luehe, J. Opt. Soc. Am. A **1**, 510 (1984).
33 M. P. Cagigal, and V. E. Canales, J. Opt. Soc. Am. A **17**, 903 (2000).
34 D. L. Fried, J. Opt. Soc. Am. **72**, 52 (1982).
35 K. G. Puschmann, and M. Sailer, Astron. Astrophys. **454**, 1011 (2006).